

Head-on collisions of Proca stars

Nicolas Sanchis-Gual,¹ Carlos Herdeiro,² José A. Font,^{1,3} and Eugen Radu²

¹*Departamento de Astronomía y Astrofísica, Universitat de València,
Dr. Moliner 50, 46100, Burjassot (València), Spain*

²*Departamento de Física da Universidade de Aveiro and Centre for Research and Development
in Mathematics and Applications (CIDMA), Campus de Santiago, 3810-183 Aveiro, Portugal*

³*Observatori Astronòmic, Universitat de València,
C/ Catedrático José Beltrán 2, 46980, Paterna (València), Spain*

(Dated: June 2018)

Proca stars, *aka* vector boson stars, are self-gravitating Bose-Einstein condensates obtained as numerical stationary solutions of the Einstein-(complex)-Proca system. These solitonic objects can achieve a compactness comparable to that of black holes, thus yielding an example of a black hole mimicker, which, moreover, can be both stable and form dynamically from generic initial data by the mechanism of gravitational cooling. In this paper we further explore the dynamical properties of these solitonic objects by performing head-on collisions of equal mass Proca stars, using fully non-linear numerical evolutions. We show that the end point and the gravitational waveform from these collisions depends on the compactness of the Proca star. Proca stars with sufficiently small compactness collide emitting gravitational radiation and leaving a stable Proca star remnant. But more compact Proca stars collide to form a transient *hypermassive* Proca star, which ends up decaying into a black hole, albeit temporarily surrounded by Proca quasi-bound states. The unstable intermediate stage can leave an imprint in the waveform, making it distinct from that of a head-on collision of black holes. The final quasi-normal ringing matches that of Schwarzschild black hole, even though small deviations may occur, as a signature of sufficiently non-linear and long-lived Proca quasi-bound states.

PACS numbers: 95.30.Sf, 04.70.Bw, 04.40.Nr, 04.25.dg

I. INTRODUCTION

The recent spectacular detections of gravitational waves [1–6] opened up a new window into the strong-field regime of gravity. Even though the data so far is well fitted by the expected physics – *i.e.* collision of Kerr black holes (BHs) or neutron stars – it is important to understand if alternative, non-conventional models of compact objects can also fit the data (*i.e.* the level of degeneracy) or how much these can be ruled out by current/future data - see [7] for such a discussion. In the best-case scenario, obtaining gravitational waveforms of such non-conventional objects could lead to their future discovery, and the exciting prospect of unveiling new surprising physics via the gravitational-wave window.

Amongst such exotic models, self-gravitating solitons composed of complex (boson stars [8]) or real (oscillatons [9]) scalar fields are some of the most dynamically studied cases - see *e.g.* [10]. Dynamical studies include, in particular, the generation of waveforms for head-on collisions of boson stars [11, 12] and oscillations [13–15]. Even if the orbital merger of such compact objects is the astrophysically more likely scenario [16, 17], and constitutes a possible mechanism to form spinning boson stars or Kerr BHs with scalar hair [18, 19], the head-on collision represents a first step to compute the gravitational waveforms produced by these objects, allowing a simpler comparison to those produced in head-on collisions of BHs or neutron stars.

It has been recently found that a complex Proca field

can form *Proca stars* (PSs), vector analogues of the scalar boson stars. PSs were constructed as static or stationary solutions of the Einstein-(complex)Proca system [20] - see also [21–24] for generalizations. Similarly to their scalar cousins, they can be regarded as single frequency, macroscopic, self-gravitating (vector) Bose-Einstein condensates. This frequency appears as a harmonic time dependence for the Proca potential and the domain of existence of PSs is very similar to that of scalar boson stars - see *e.g.* Fig. 1 in [25] - except that the latter have a smaller maximal mass and a wider frequency range.

Several dynamical aspects of the gravitational interaction of Proca fields have been addressed in recent years, using numerical studies. Long-lived, quasi-bound states of Proca fields around Schwarzschild BHs have been considered in [26, 27] (see also [28]). The superradiant instability of Kerr BHs was triggered by Proca fields in [29, 30], leading, in particular, to the formation of Kerr BH with Proca hair [21, 31]. In [32] fully non-linear evolutions of PSs were performed, to assess their stability. The simulations showed the existence of a stable branch (connecting the vacuum with the solution with maximal ADM mass) and an unstable branch. Solutions belonging to the latter may have different fates, depending on the initial perturbation and the sign of their binding energy. As their scalar cousins, with and without a self-interacting term [33–36], unstable solutions with positive binding energy migrate to the stable branch, whereas unstable solutions with a negative binding energy (excess energy) undergo fission; *i.e.* they disperse entirely. Both cases can also collapse to form

a Schwarzschild BH. More recently, additional numerical simulations [37] have shown that PS can also form dynamically from generic initial data describing a non-compact “cloud” of the Proca field, through the so called gravitational cooling mechanism, first described in the 1990s in the context of scalar boson stars [38].

In this work we shall continue the exploration of the dynamics of PSs by performing numerical evolutions describing head-on collisions of PS binaries and computing the gravitational radiation emitted. The results we obtain parallel qualitatively those for head-on collisions of scalar boson (or even oscillaton) stars. For sufficiently small compactness, or equivalently, low mass in units of the Proca field mass – see Fig. 1 below – the collisions form a more massive, but still stable, PS, not a BH. The final star is, however, perturbed and in the timescale of our simulations it only partially relaxes to equilibrium. Sufficiently compact PSs, on the other hand, form a horizon when colliding, but only after an intermediate phase that could be described as a *hypermassive* PS. This intermediate stage leaves an imprint in the waveform, making it distinct from that of a head-on collision of Schwarzschild BHs. After horizon formation the BH ringdown can be seen, which matches well that of a Schwarzschild BH. But in the cases where a larger Proca remnant remains outside the horizon, in the form of Proca quasi-bound states, we observe a difference with the BH ringdown. A similar observation was reported recently in the study of head-on collisions of oscillaton stars [15].

This paper is organized as follows. In Section II we present the equations of the Einstein-(complex)Proca model that will be used for the numerical evolutions. In Section III we present the initial data that will be used in our numerical evolutions. A brief description of the numerical techniques is given in Section IV and our results are presented in Section V. Final remarks are presented in Section VI. A brief assessment of the numerical code is given in Appendix A.

II. BASIC EQUATIONS

We shall investigate the dynamics of a complex Proca field by solving numerically the Proca equations coupled to the Einstein equations. The system is described by the action $\mathcal{S} = \int d^4x \sqrt{-g} \mathcal{L}$, where the Lagrangian density depends on the Proca potential \mathcal{A} , and field strength $\mathcal{F} = d\mathcal{A}$; it is given by:

$$\mathcal{L} = \frac{R}{16\pi G} - \frac{1}{4} \mathcal{F}_{\alpha\beta} \bar{\mathcal{F}}^{\alpha\beta} - \frac{1}{2} \mu^2 \mathcal{A}_\alpha \bar{\mathcal{A}}^\alpha, \quad (1)$$

where the bar denotes complex conjugation, R is the Ricci scalar, G is Newton’s constant and μ is the Proca field mass. The stress-energy tensor of the Proca field

reads

$$T_{ab} = -\mathcal{F}_{c(\alpha} \bar{\mathcal{F}}_{b)}^c - \frac{1}{4} g_{ab} \mathcal{F}_{cd} \bar{\mathcal{F}}^{cd} + \mu^2 \left[\mathcal{A}_{(\alpha} \bar{\mathcal{A}}_{b)} - \frac{1}{2} g_{ab} \mathcal{A}_c \bar{\mathcal{A}}^c \right]. \quad (2)$$

Using the standard 3+1 split (see *e.g.* [32] for more details) the Proca field is split into 3+1 quantities:

$$\mathcal{A}_\mu = \mathcal{X}_\mu + n_\mu \mathcal{X}_\phi, \quad (3)$$

$$\mathcal{X}_i = \gamma_i^\mu \mathcal{A}_\mu, \quad (4)$$

$$\mathcal{X}_\phi = -n^\mu \mathcal{A}_\mu, \quad (5)$$

where \mathcal{X}_i is the vector potential and \mathcal{X}_ϕ is the scalar potential. The fully non-linear Einstein-Proca system reads:

$$\partial_t \gamma_{ij} = -2\alpha K_{ij} + \mathcal{L}_\beta \gamma_{ij}, \quad (6)$$

$$\partial_t \mathcal{X}_i = -\alpha (E_i + D_i \mathcal{X}_\phi) - \mathcal{X}_\phi D_i \alpha + \mathcal{L}_\beta \mathcal{X}_i, \quad (7)$$

$$\partial_t E^i = \alpha (K E^i + D^i Z + \mu_V^2 \mathcal{X}^i + \epsilon^{ijk} D_j B_k) - \epsilon^{ijk} B_j D_k \alpha + \mathcal{L}_\beta E^i, \quad (8)$$

$$\begin{aligned} \partial_t K_{ij} = & -D_i D_j \alpha + \alpha (R_{ij} - 2K_{ik} K^k_j + K K_{ij}) \\ & + 2\alpha \left(E_i E_j - \frac{1}{2} \gamma_{ij} E^k E_k + B_i B_j \right. \\ & \left. - \frac{1}{2} \gamma_{ij} B^k B_k - \mu_V^2 \mathcal{X}_i \mathcal{X}_j \right) + \mathcal{L}_\beta K_{ij}, \end{aligned} \quad (9)$$

$$\begin{aligned} \partial_t \mathcal{X}_\phi = & -\mathcal{X}^i D_i \alpha + \alpha (K \mathcal{X}_\phi - D_i \mathcal{X}^i - Z) \\ & + \mathcal{L}_\beta \mathcal{X}_\phi, \end{aligned} \quad (10)$$

$$\partial_t Z = \alpha (D_i E^i + \mu_V^2 \mathcal{X}_\phi - \kappa Z) + \mathcal{L}_\beta Z, \quad (11)$$

where α is the lapse function, β is the shift vector, γ_{ij} is the spatial metric, K_{ij} is the extrinsic curvature (with $K = K^i_i$), D_i is the covariant 3-derivative, and \mathcal{L}_β is the Lie derivative. Moreover, the three-dimensional “electric” E^i and “magnetic” B^i fields are also introduced in the previous equations. The system is solved using the time-evolution numerical code from [27] (see Section IV).

III. INITIAL DATA

PSs were obtained in [20] as stationary solutions to the model described by the action (1). Four illustrative examples of spherically symmetric PSs will be taken as the initial data for our time evolutions. Their basic physical properties, frequency, w , ADM mass, M_{ADM} , Noether charge Q and the Proca “electric” potential at the origin, Φ_c , all in units of the vector field mass, can be found in Table I and their distribution in an ADM mass *vs.* Proca field frequency diagram is shown in Fig. 1.

When computed as static solutions [20], spherically symmetric PSs are given by the line element

$$ds^2 = -e^{2F_0} dt^2 + e^{2F_1} [dr^2 + r^2 (d\theta^2 + \sin^2 \theta d\varphi^2)], \quad (12)$$

TABLE I: Spherically symmetric Proca star models.

Model	w/μ	μM_{ADM}	$\mu^2 Q$	$\Phi_c(r=0)$
PS0	0.97	0.693	0.702	0.0087
PS1	0.95	0.849	0.864	0.0214
PS2	0.90	1.036	1.063	0.0779
PS3	0.85	1.039	1.065	0.2121

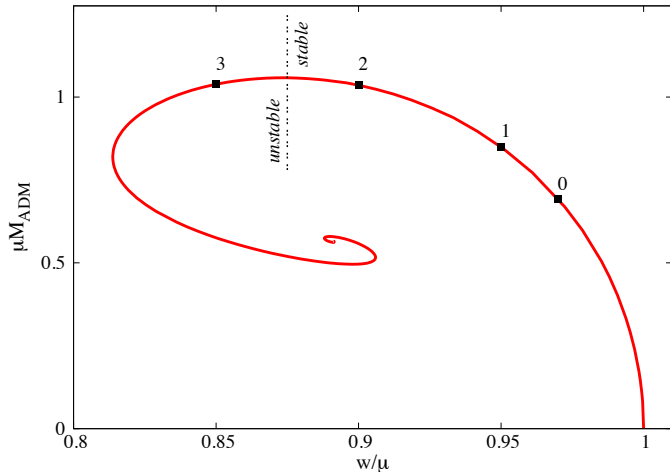


FIG. 1: Domain of existence of the spherical (fundamental) PS solutions (solid line) in an ADM mass $vs.$ vector field frequency diagram. We highlight the four solutions used in the head-on collisions in this work.

where F_0, F_1 are radial functions and r, θ, φ correspond to isotropic coordinates. The Proca field ansatz is given in terms of another two real functions (V, H_1) which depend also on r

$$\mathcal{A} = e^{-i\omega t} \left(iV dt + \frac{H_1}{r} dr \right), \quad (13)$$

where $w > 0$ is the frequency of the field. The translation between the four radial functions above, F_0, F_1, V, H_1 , and the initial value for the metric and the 3+1 Proca field variables described is given as follows:

$$\alpha = e^{F_0}, \quad (14)$$

$$\gamma_{rr} = e^{2F_1}, \gamma_{\theta\theta} = e^{2F_1} r^2, \gamma_{\phi\phi} = e^{2F_1} r^2 \sin^2 \theta, \quad (15)$$

$$\mathcal{X}_\phi = -n^\mu \mathcal{A}_\mu, \quad (16)$$

$$\mathcal{X}_i = \gamma_i^\mu \mathcal{A}_\mu, \quad (17)$$

$$E^i = -i \frac{\gamma^{ij}}{\alpha} \left(D_j(\alpha \mathcal{X}_\phi) + \partial_t \mathcal{X}_j \right). \quad (18)$$

We follow [11] to construct appropriate initial data to study the head-on collision of these compact objects. We take a superposition of two PS solutions:

- $\mathcal{A}(x_i) = \mathcal{A}^{(1)}(x_i - x_0) + \mathcal{A}^{(2)}(x_i + x_0)$,
- $\gamma_{ij}(x_i) = \gamma_{ij}^{(1)}(x_i - x_0) + \gamma_{ij}^{(2)}(x_i + x_0) - \gamma_{ij}^{\text{flat}}(x_i)$,

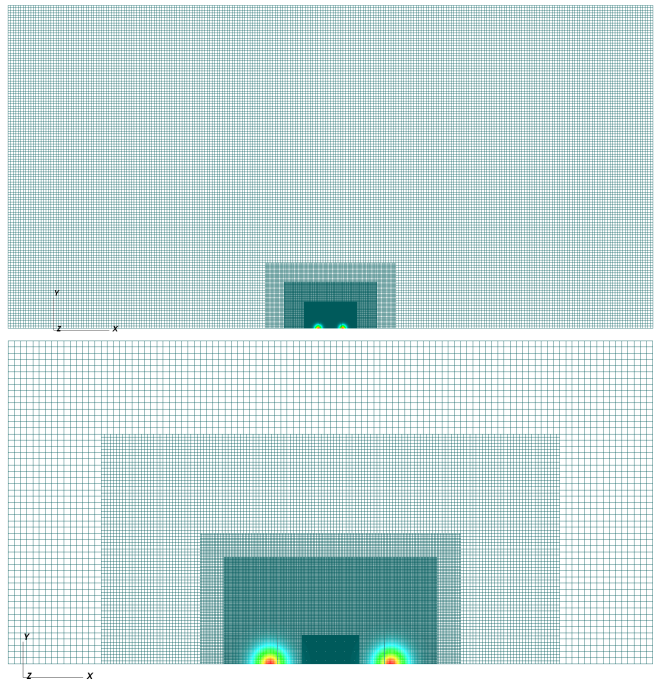


FIG. 2: Computational mesh-refined grid used for the evolutions. The top panel shows the entire domain while the bottom panel is a magnification of the inner region.

$$\bullet \alpha(x_i) = \alpha^{(1)}(x_i - x_0) + \alpha^{(2)}(x_i + x_0) - 1,$$

where superindex (i) labels the stars and $\pm x_0$ indicates their initial positions. The stars are initially separated by $\Delta x = 39$, which corresponds to $x_0 = \pm 19.5$ (in $G = c = 1$ units). The solutions are not boosted. These initial data introduce constraint violations. However, they are small and do not grow during the evolution, as we discuss in Appendix A.

IV. NUMERICS

To perform the numerical evolutions we use the freely available `Einstein Toolkit` [39, 40], which uses the `Cactus` framework and mesh refinement. The method-of-lines is employed to integrate the time-dependent differential equations. In particular, we use a fourth-order Runge-Kutta scheme for this task. The left-hand-side of the Einstein equations is solved using the `MacLachlan` code [41, 42], which is based on the 3+1 Baumgarte-Shapiro-Shibata-Nakamura (BSSN) formulation.

The Proca evolution equations, Eqs. (6)-(11), are solved using the code developed independently by M. Zilhão and H. Witek [27]. We have extended this code to take into account a complex field. All technical details, assessment of the code and convergence tests can be found in [27].

We use a numerical grid with 6 refinement levels, its structure being $\{(512, 64, 64, 32, 32, 8), (4, 2, 1, 0.5, 0.25, 0.125)\}$, where the first set of numbers

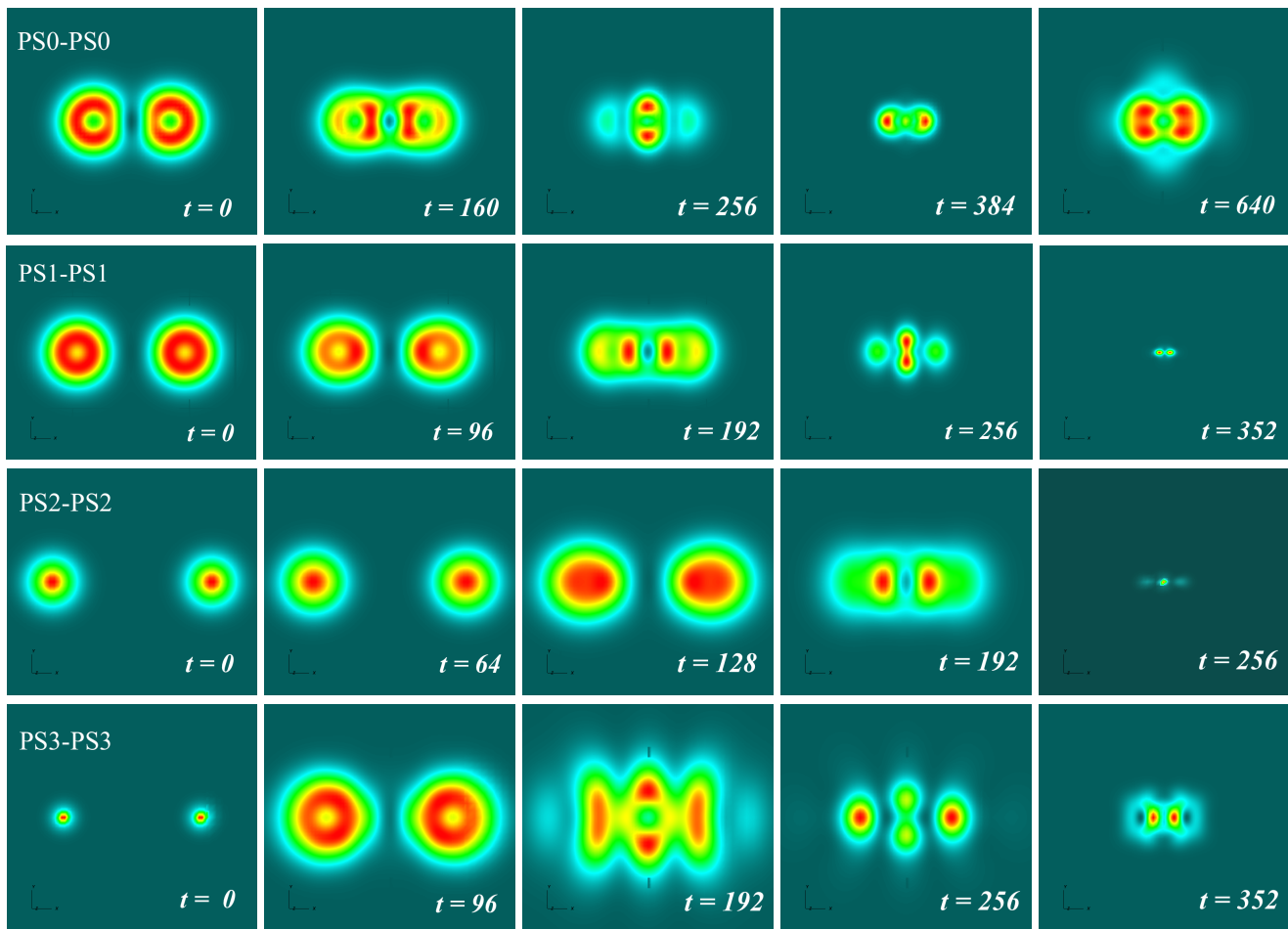


FIG. 3: Snapshots of the energy density for PS0-PS0, PS1-PS1, PS2-PS2 and PS3-PS3 in the equatorial plane. The vertical axis correspond to the y direction and the horizontal to the x direction.

indicates the spatial domain of each level and the second set indicates the resolution. Fig. 2 shows the grid structure at $t = 0$. The outer boundary is located at $\Delta x = 392$ from the extraction radii. This ensures that the total time of the simulations is shorter than twice the light-crossing time, which prevents numerical reflections at the boundary from affecting the extraction. Due to the geometry of head-on collisions, we consider equatorial-plane symmetry and reflection symmetry with respect to the x - z plane.

V. RESULTS

We evolve the initial data described in Section III for four equal-mass PS binaries, using the four types of PSs described in Table I and highlighted in Fig. 1. We label these four models as PS0-PS0, PS1-PS1, PS2-PS2, and PS3-PS3. We also evolve the latter including an initial perturbation which consists in multiplying by a number slightly larger than one the initial values of the Proca variables, as we did in [32], a model that we dub PS3b-

PS3b. By including a perturbation the stars are forced to collapse before the collision, since the PS3 model is unstable against radial perturbations.

A. Visualisation of the collisions

Fig. 3 shows equatorial-plane snapshots of the evolutions of the PS0-PS0, PS1-PS1, PS2-PS2 and PS3-PS3 binaries, from top to bottom. Our computational grid only extends from $y = 0$ to 512, therefore the data for negatives values of y are mirrored by the corresponding positive y values, due to axisymmetry. Animations illustrating these collisions can be found in [43].

The collision of the two Proca stars happens at $t \sim 160$ for models PS0-PS0 and PS3-PS3, and at $t \sim 192$ for PS1-PS1 and PS2-PS2. The merged object oscillates in the x and y directions. For PS0-PS0, part of the field is ejected from the polar caps and approaches spherical symmetry. Model PS2-PS2 collapses quickly after the collision at $t_{\text{collapse}} \sim 245$, while models PS1-PS1 and PS3-PS3 oscillate during a short period of time before

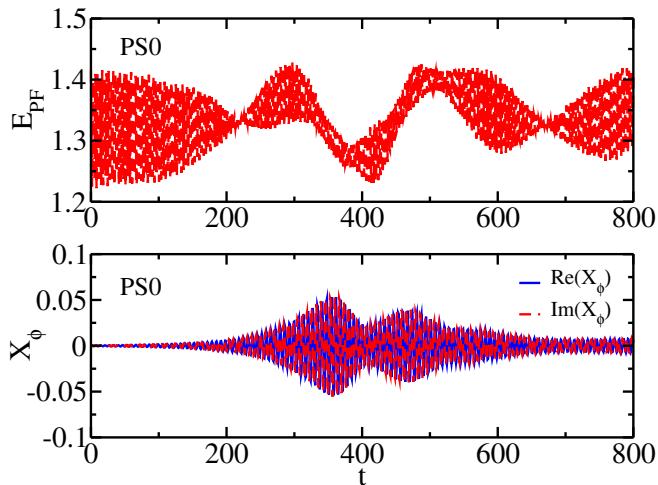


FIG. 4: Model PS0-PS0. Time evolution of the Proca field energy (top panel) and of the amplitude of the real and imaginary parts of the scalar potential extracted at $r = 0$ (bottom panel).

an apparent horizon (AH) appears at $t_{\text{collapse}} \sim 375$ and $t_{\text{collapse}} \sim 425$, respectively. Moreover, the PS1-PS1 collision forms a perturbed massive PS that oscillates and produces the first part of the gravitational wave signal, as we show below. In the case of PS3-PS3, the stars migrate and expand before the collision. For all models, the morphology and amplitude of the gravitational waves are clearly influenced by the dynamics during the collision (cf. Section V C).

B. Proca energy and horizon formation

In Fig. 4 we plot the time evolution of the Proca field energy

$$E_{\text{PF}} = - \int_{\Sigma} dr d\theta d\varphi (2T_t^t - T_\alpha^\alpha) \alpha \sqrt{\gamma}, \quad (19)$$

and of the amplitude of the real and imaginary parts of the time component of the Proca 4-potential (hereafter the “scalar” potential) for model PS0-PS0. In this case we see no horizon formation. The stars have sufficiently low mass so that the final state is still a star. The amplitude of the scalar potential stabilises within the timescale of our simulation. It has been reported in [13, 15] that some collapsed oscillatons from head-on collisions can lose part of the field and form a stable, less compact oscillaton, not collapsing to a BH even if the total mass is larger than the maximum mass of the equilibrium configuration. This seems to be precisely what is occurring for model PS0-PS0. The mass of the PS0 Proca star is $\mu M_{\text{ADM}} = 0.693$, so that twice that mass is larger than the maximum mass for spherical PSs, which is $\mu M_{\text{ADM}}^{\text{max}} = 1.058$ [20]. Still, a PS forms, as a result of the inelasticity of the collision.

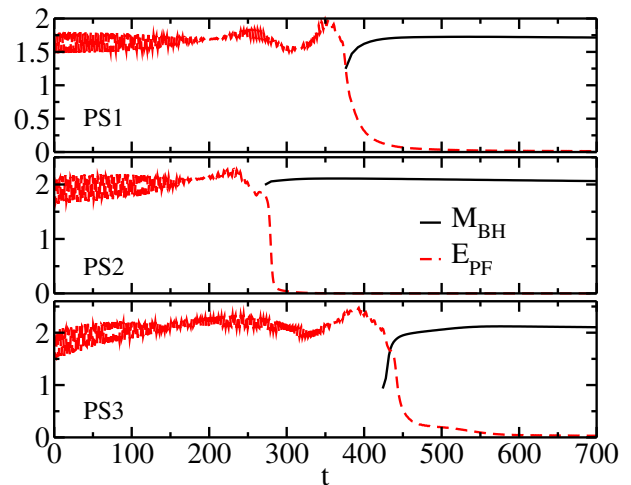


FIG. 5: Time evolution of the Proca field energy and BH mass for models PS1-PS1 (top panel), PS2-PS2 (middle panel) and PS3-PS3 (bottom panel).

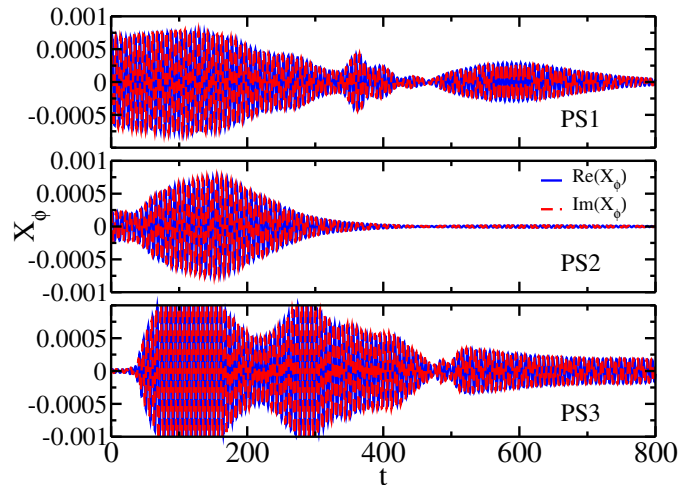


FIG. 6: Time evolutions of the amplitude of the real and imaginary parts of the scalar potential extracted at $r = 12$ for models PS1-PS1 (top panel), PS2-PS2 (middle panel) and PS3-PS3 (bottom panel).

Fig. 5 displays the time evolution of the Proca field energy and of the irreducible mass of the AH for models PS1-PS1, PS2-PS2 and PS3-PS3. For these three models, the collapse of the solutions is triggered after the collision and an AH forms. After the collapse there is still a Proca field remnant outside the horizon, as Fig. 6 shows. For PS1-PS1 and PS3-PS3 this remnant has a visible dynamics, reminiscent of a beating pattern, a signature of the presence of more than one quasi-bound state outside the AH. In the case of the PS3-PS3 model, the Proca remnant seems particularly long lived. We shall observe a possible impact of this feature in the gravitational waveform below.

C. Waveforms

In Figs. 7 and 8 we plot the resulting gravitational waveforms, showing the Newman-Penrose scalar $r\Psi_4^{l=2,m}$, for the modes $l=2$, $m=\{0,+2\}$, extracted at radii $r_{\text{ext}}=\{100,120\}$. The waves, conveniently shifted and rescaled, overlap, as expected in the wave zone. Non-axisymmetric modes $l=2$, $m=\pm 1$ are consistent with zero. In agreement with the results for head-on collisions of spherical boson stars in [11], we find that the coefficients $\mathcal{C}_{2,m}$ of the different modes are related in the following way:

$$\text{Re}(\mathcal{C}_{2,+2}) = \text{Re}(\mathcal{C}_{2,-2}), \quad (20)$$

$$\text{Re}(\mathcal{C}_{2,+2}) = -\sqrt{3/2} \text{Re}(\mathcal{C}_{2,0}). \quad (21)$$

For our sample of models, the amplitude of the gravitational waves increases monotonically with decreasing vector-field frequency. The largest amplitude is achieved for model PS3-PS3 which is more than an order of magnitude larger than for model PS0-PS0. All waveforms are of the burst-type, of which PS2-PS2 and PS3-PS3 are clear examples. Morphological differences are apparent in model PS0-PS0 and, in particular in model PS1-PS1. For the latter, plotted in the middle panels of Fig. 7, there is a time delay $\Delta t \sim 100$ between the first negative peak of the waveform (at around $t \sim 275$) and the collapse (at around $t \sim 375$). The waveform can be regarded as composed by two contributions: the first part, from $t \sim 250$ to $t \sim 375$, would correspond to the collision of the stars, forming a “hypermassive” PS, a remnant that oscillates and eventually collapses to a BH at $t \sim 375$, triggering the second part of the wave. The collapse nearly coincides with a peak of the waveform and the corresponding time is highlighted by a vertical dashed line in the figure. For PS2-PS2 and PS3-PS3, these dynamics are absent, the AHs form promptly and their times of formation are very close to the first positive peak in the waveforms (vertical dashed lines).

The bottom panels of Fig. 8 show the gravitational waveform for the PS3b-PS3b model together with those of models PS2-PS2 and PS3-PS3. Recall that PS2 and PS3 have almost the same mass (less than 1% difference), therefore the BH formed will have a similar mass. Thus, we can compare the quasinormal modes (QNMs) of the three cases. For PS2-PS2, the QNMs are in good agreement in at least four of the peaks, while for PS3-PS3 there are some differences in the frequency. This comparison becomes more clear in the QNM ringdown plots shown in Fig. 9, where we plot the waveforms in logarithmic scale and we fit them to the QNMs of a Schwarzschild BH, following the results of [44]. PS2-PS2, PS3-PS3 and PS3b-PS3b have almost the same total mass, therefore the fit is the same. The agreement for PS2-PS2 and PS3b-PS3b is very good. The masses that we obtain from the fits have an error of 7% for PS1-PS1 and 4% for PS2-PS2, PS3-PS3 and PS3b-PS3b, with respect to the masses computed with the `AHFinder` algorithm of the `Einstein Toolkit`.

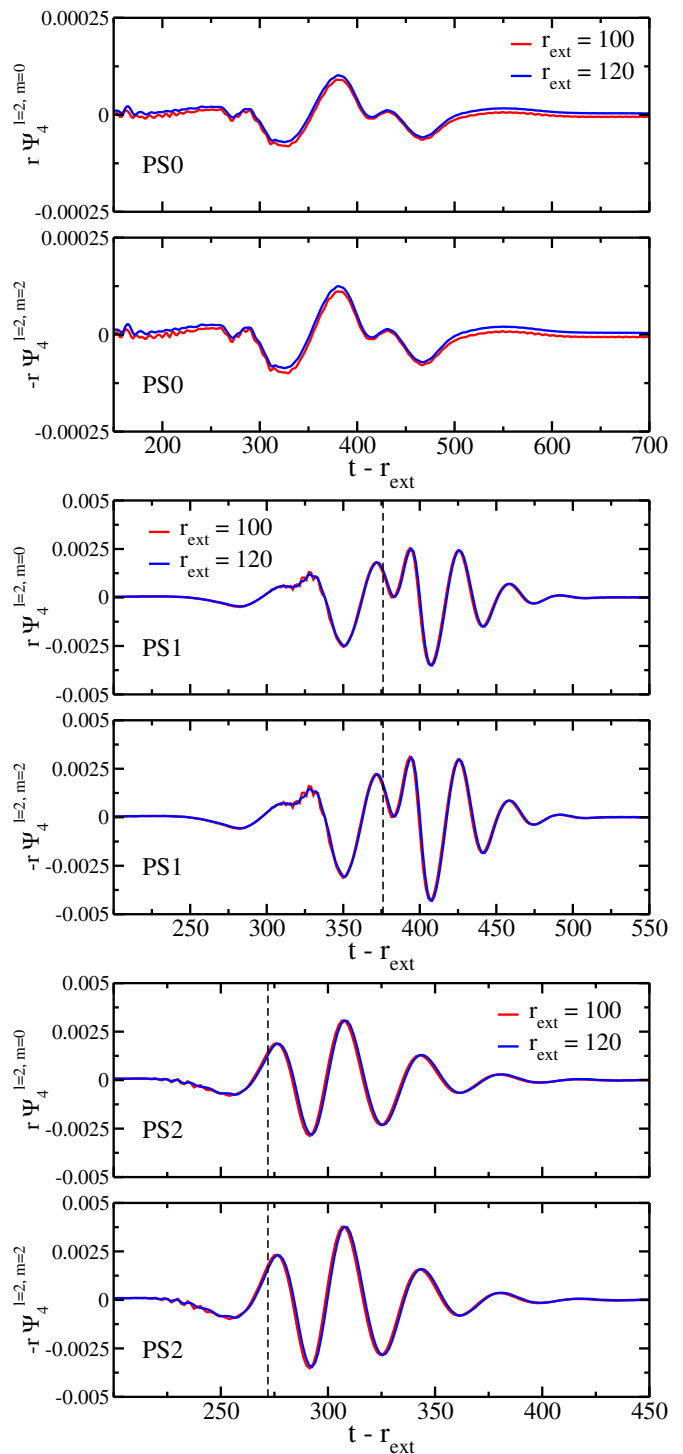


FIG. 7: Real part of $r\Psi_4^{l=2,m=0}$ and $r\Psi_4^{l=2,m=+2}$ for PS0-PS0 (top panels), PS1-PS1 (middle panels) and PS2-PS2 (bottom panels).

However, for the PS3-PS3 waveform the frequency does not match the PS3b-PS3b nor the QNM fit. A possible interpretation is that this is due to the fact that there is still a rich Proca field environment around the newly form BH, *cf.* Figs. 5 and 6.

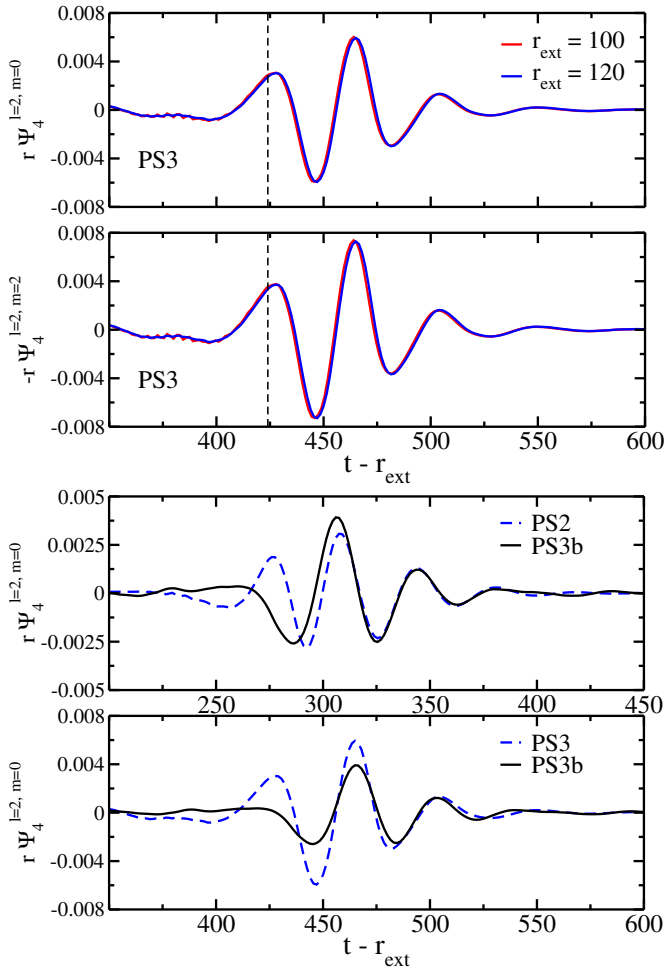


FIG. 8: Real part of $r\Psi_4^{l=2, m=0}$ and $r\Psi_4^{l=2, m=+2}$ for PS3-PS3 (top panels). Comparison of the real part of $r\Psi_4^{l=2, m=0}$ between PS2-PS2, PS3-PS3 and PS3b-PS3b computed at $r_{\text{ext}} = 120$. The latter is conveniently time shifted (bottom panels).

D. Comparison with BH collisions

We also perform head-on collisions of Schwarzschild BHs with the same mass as the PSs in each model. This allows to compare the resulting gravitational waveforms with those from the PS binaries. The real part of $r\Psi_4^{l=2, m=0}$ for both cases is shown in Fig. 10. Observe that for model PS3b-PS3b, we obtain essentially the same gravitational waveform. This is the expected result; in this case, the PSs collapse to BHs before the actual collision due to the initial perturbation we have imposed, thus leading to a head-on collision of BHs. In the case of PS2-PS2, the ringdown phase overlap almost perfectly that same phase for the BH collision in agreement with the QNMs analysis in Fig. 9. The first part of the wave, however, is different: the frequency is higher but the amplitude is slightly smaller at the peak of the emission.

On the other hand, as already shown in the previous

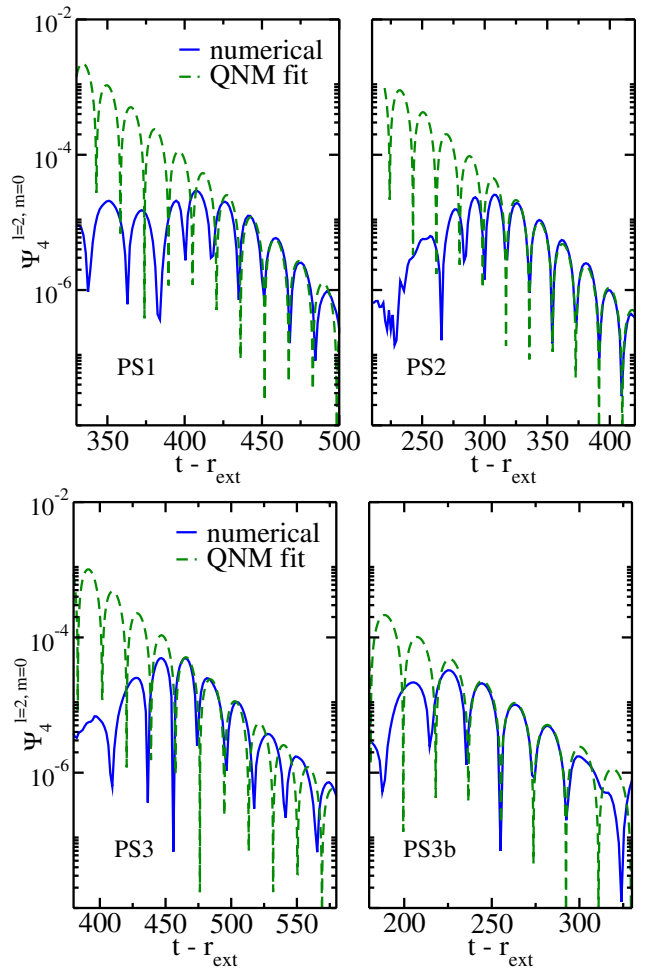


FIG. 9: Black hole ringing and quasinormal modes (QNMs) for models PS1-PS1 (top left panel), PS2-PS2 (top right panel), PS3-PS3 (bottom left panel), and PS3b-PS3b (bottom right panel). The QNM fit shown for PS2-PS2, PS3-PS3 and PS3b-PS3b corresponds to the same BH mass. All waveforms are computed at $r_{\text{ext}} = 120$.

subsection, for PS1-PS1 and PS3-PS3, the comparison indicates that the waveforms depart from those of the Schwarzschild BH collisions. The amplitudes are different for both models. Some of the QNM oscillations can be fitted with the Schwarzschild BH-BH waveforms but not all, as the frequency changes, see Fig. 11. The deviation in the frequency could be a signature of the presence of quasi-bound states around the BH and might be in particular related to the compactness of the remaining Proca field around the BH. The gravitational radiation induced by accreting shells of matter evolving in fixed BH backgrounds was first studied in [45] by numerically solving the linearized curvature perturbation equations (see also [46] for a dynamical spacetime study). It was found that the excitation of the BH QNM ringing strongly depends on the shell thickness, becoming increasingly clear with progressively more compact shells (see Fig. 10 in [45]). In the infinitesimally thin limit, the

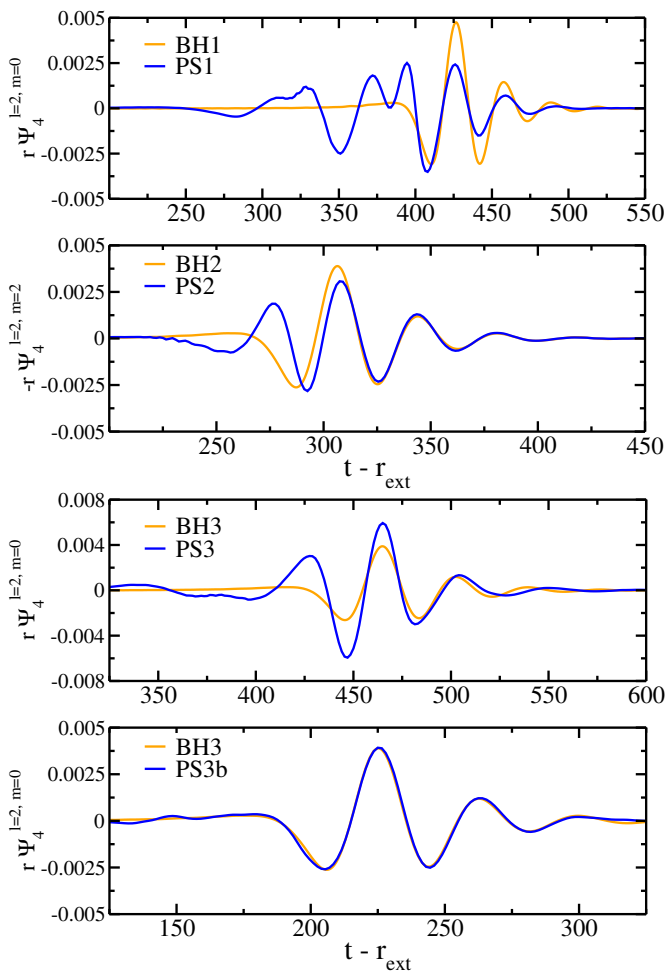


FIG. 10: Comparison of the real part of $r\Psi_4^{|l|=2, m=0}$ computed at $r_{ext} = 120$ from head-on collisions of PSs (blue lines) and Schwarzschild BHs of the same mass (orange lines).

gravitational energy asymptotes to a finite value, about a third of the point particle upper limit. Those findings confirmed earlier ideas about the QNM excitation mechanism made by [47], namely that the *strong* excitation is induced by curvature profiles that have spatial wavelengths comparable to the width of the BH potential.

VI. CONCLUSIONS

In this paper we have used numerical-relativity techniques to study the head-on collision of (equal ADM mass and vector field frequency) Proca stars and extract the gravitational radiation produced in the collision. PSs are macroscopic, self-gravitating, Bose-Einstein condensates built out of a massive, complex, vector field [20]. Since they can achieve a compactness comparable to that of BHs, they are a type of BH mimicker with appealing dynamical properties, namely they are stable against perturbations [20, 32] and they can form dynamically through a gravitational cooling mechanism [37].

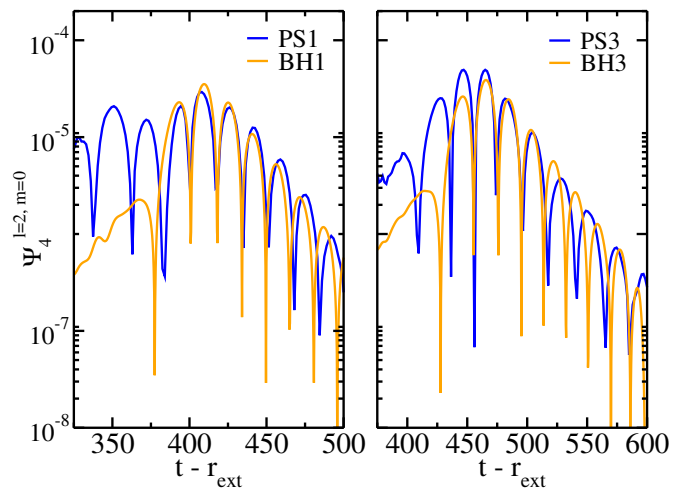


FIG. 11: Black hole ringing and quasinnormal modes (QNMs) for models PS1-PS1 and the corresponding BH binary with the same mass (left panel). Same for PS3-PS3 (right panel).

The collision of these spherically symmetric solutions may lead either to the formation of a more massive PS, which we dub “hypermassive” PS or, if the initial PSs are sufficiently massive/compact, to the formation of a Schwarzschild BH. Horizon formation, however, only occurs after an intermediate phase, which leaves an imprint in the waveform, making it distinct from that of a head-on collision of Schwarzschild BHs. After horizon formation the BH QNMs match those of a Schwarzschild BH. However, we have found that for those cases where the final BH is surrounded by a sufficiently extended and long-lived quasi-stationary Proca cloud, differences with the BH ringdown are noticeable.

The head-on collisions of PSs discussed in this paper are a first step before attempting realistic binary mergers incorporating orbital dynamics. Such a study is underway and results will be presented elsewhere.

Acknowledgements

NSG thanks Miguel Zilhão and Vassilios Mewes for useful discussions. This work has been supported by the Spanish MINECO (grant AYA2015-66899-C2-1-P), by the Generalitat Valenciana (PROMETEOII-2014-069, ACIF/2015/216), by the FCT (Portugal) IF programme, by the CIDMA (FCT) strategic project UID/MAT/04106/2013 and by the European Union’s Horizon 2020 research and innovation (RISE) programmes H2020-MSCA-RISE-2015 Grant No. StronGrHEP-690904 and H2020-MSCA-RISE-2017 Grant No. FunFiCO-777740. The authors would like to acknowledge networking support by the COST Action CA16104. Computations have been performed at the Servei d’Informàtica de la Universitat de València.

Appendix A: Code assessment

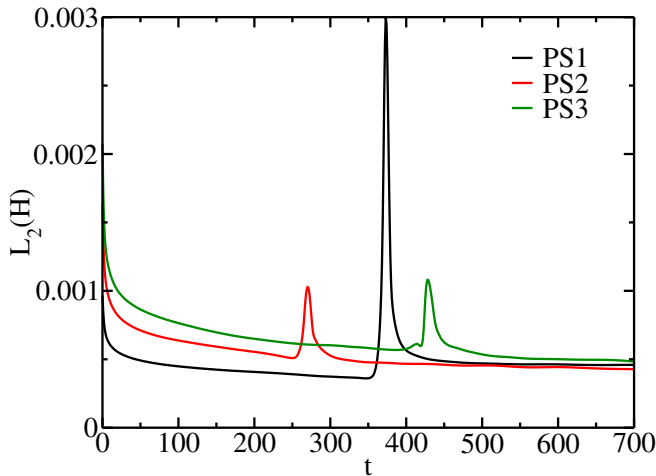


FIG. 12: L_2 -norm of the Hamiltonian constraint for PS1-PS1, PS2-PS2 and PS3-PS3.

We briefly comment here on the standard analyses

we carried out to assess the quality of our simulations with the `Einstein Toolkit`. In Fig. 12 we show the behaviour of the L_2 -norm of the Hamiltonian constraint. The floor of the violation of this constraint is at $\sim 4 \times 10^{-4}$ during most of the simulation. A significant peak in the violations of the constraint appears when the BH forms, but the errors quickly decrease to the pre-collision values and remain stable during the rest of the simulation.

In Fig. 13 we plot the gravitational wave of the PS2-PS2 and the PS3-PS3 cases for three different resolutions. The grid structure is $\{(512, 64, 64, 32, 32, 8), (8, 4, 2, 1, 0.5, 0.25)\}$ and $\{(512, 64, 64, 32, 32, 8), (16, 8, 4, 2, 1, 0.5)\}$ for medium and low resolution, respectively. The high resolution is the one used in the simulations shown in this paper. For PS2-PS2, the results for the three resolutions converge. For the PS3-PS3 model the low resolution is not good enough to allow us to extract the gravitational waveform. The medium and high resolutions provide adequate results showing that they are in the convergence regime.

- [1] B. P. Abbott, R. Abbott, T. D. Abbott, M. R. Abernathy, F. Acernese, K. Ackley, C. Adams, T. Adams, P. Addesso, R. X. Adhikari, et al., *Physical Review Letters* **116**, 061102 (2016), 1602.03837.
- [2] B. P. Abbott et al. (Virgo, LIGO Scientific), *Phys. Rev. Lett.* **116**, 241103 (2016), 1606.04855.
- [3] B. P. Abbott et al. (VIRGO, LIGO Scientific), *Phys. Rev. Lett.* **118**, 221101 (2017), 1706.01812.
- [4] B. P. Abbott et al. (Virgo, LIGO Scientific), *Phys. Rev. Lett.* **119**, 141101 (2017), 1709.09660.
- [5] B. P. Abbott et al. (Virgo, LIGO Scientific), *Astrophys. J.* **851**, L35 (2017), 1711.05578.
- [6] B. Abbott et al. (Virgo, LIGO Scientific), *Phys. Rev. Lett.* **119**, 161101 (2017), 1710.05832.
- [7] N. K. Johnson-McDaniel, A. Mukherjee, R. Kashyap, P. Ajith, W. Del Pozzo, and S. Vitale (2018), 1804.08026.
- [8] F. E. Schunck and E. W. Mielke, *Class. Quant. Grav.* **20**, R301 (2003), 0801.0307.
- [9] E. Seidel and W. M. Suen, *Phys. Rev. Lett.* **66**, 1659 (1991).
- [10] S. L. Liebling and C. Palenzuela, *Living Rev. Rel.* **15**, 6 (2012), 1202.5809.
- [11] C. Palenzuela, I. Olabarrieta, L. Lehner, and S. L. Liebling, *Physical Review D* **75**, 064005 (2007).
- [12] V. Cardoso, S. Hopper, C. F. Macedo, C. Palenzuela, and P. Pani, *Physical review D* **94**, 084031 (2016).
- [13] R. Brito, V. Cardoso, and H. Okawa, *Physical review letters* **115**, 111301 (2015).
- [14] R. Brito, V. Cardoso, C. F. Macedo, H. Okawa, and C. Palenzuela, *Physical Review D* **93**, 044045 (2016).
- [15] T. Helfer, E. A. Lim, M. A. Garcia, and M. A. Amin, *arXiv preprint arXiv:1802.06733* (2018).
- [16] C. Palenzuela, L. Lehner, and S. L. Liebling, *Physical Review D* **77**, 044036 (2008).

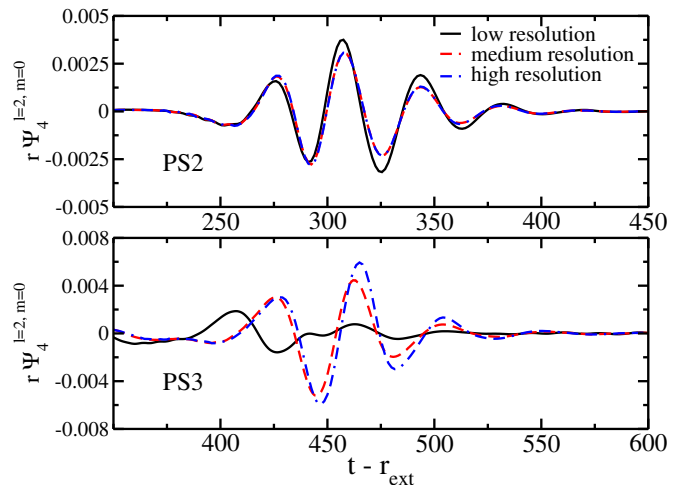


FIG. 13: Resolution comparison for the gravitational wave extracted at $r_{\text{ext}} = 120$ for PS2-PS2 (top panel) and PS3-PS3 (bottom panel).

- [17] M. Bezares, C. Palenzuela, and C. Bona, *Physical Review D* **95**, 124005 (2017).
- [18] C. A. R. Herdeiro and E. Radu, *Phys.Rev.Lett.* **112**, 221101 (2014), 1403.2757.
- [19] C. Herdeiro and E. Radu, *Class. Quant. Grav.* **32**, 144001 (2015), 1501.04319.
- [20] R. Brito, V. Cardoso, C. A. R. Herdeiro, and E. Radu, *Phys. Lett.* **B752**, 291 (2016), 1508.05395.
- [21] C. Herdeiro, E. Radu, and H. Runarsson, *Class. Quant. Grav.* **33**, 154001 (2016), 1603.02687.

- [22] F. Garca and I. S. Landea (2016), 1608.00011.
- [23] M. Duarte and R. Brito, Phys. Rev. **D94**, 064055 (2016), 1609.01735.
- [24] M. Minamitsuji, Phys. Rev. **D97**, 104023 (2018), 1805.09867.
- [25] P. V. P. Cunha, J. A. Font, C. Herdeiro, E. Radu, N. Sanchis-Gual, and M. Zilhó, Phys. Rev. **D96**, 104040 (2017), 1709.06118.
- [26] H. Witek, V. Cardoso, A. Ishibashi, and U. Sperhake, Physical Review D **87**, 043513 (2013).
- [27] M. Zilhão, H. Witek, and V. Cardoso, Class. Quant. Grav. **32**, 234003 (2015), 1505.00797.
- [28] J. G. Rosa and S. R. Dolan, Phys. Rev. **D85**, 044043 (2012), 1110.4494.
- [29] W. E. East and F. Pretorius, Physical review letters **119**, 041101 (2017).
- [30] W. E. East, Physical Review D **96**, 024004 (2017).
- [31] C. A. R. Herdeiro and E. Radu, Phys. Rev. Lett. **119**, 261101 (2017), 1706.06597.
- [32] N. Sanchis-Gual, C. Herdeiro, E. Radu, J. C. Degollado, and J. A. Font, Physical Review D **95**, 104028 (2017).
- [33] E. Seidel and W.-M. Suen, Phys. Rev. **D42**, 384 (1990).
- [34] J. Balakrishna, E. Seidel, and W.-M. Suen, Phys. Rev. **D58**, 104004 (1998), gr-qc/9712064.
- [35] F. S. Guzman, Phys. Rev. **D70**, 044033 (2004), gr-qc/0407054.
- [36] A. Escorihuela-Tomás, N. Sanchis-Gual, J. C. Degollado, and J. A. Font, Physical Review D **96**, 024015 (2017).
- [37] F. Di Giovanni, N. Sanchis-Gual, C. A. Herdeiro, and J. A. Font, arXiv preprint arXiv:1803.04802 (2018).
- [38] E. Seidel and W.-M. Suen, Physical review letters **72**, 2516 (1994).
- [39] E. Toolkit, URL <http://einstein toolkit.org> (2012).
- [40] F. Löffler, Classical Quantum Gravity **29**, 115001 (2012).
- [41] D. Brown, P. Diener, O. Sarbach, E. Schnetter, and M. Tiglio, Physical Review D **79**, 044023 (2009).
- [42] C. Reisswig, C. D. Ott, U. Sperhake, and E. Schnetter, Physical Review D **83**, 064008 (2011).
- [43] <http://gravitation.web.ua.pt/node/1522>.
- [44] E. Leaver, Proc.Roy.Soc.Lond. **A402**, 285 (1985).
- [45] P. Papadopoulos and J. A. Font, Physical Review D **59**, 044014 (1999).
- [46] P. Papadopoulos and J. A. Font, Phys. Rev. D **63**, 044016 (2001), gr-qc/0009024.
- [47] Y. Sun and R. H. Price, Phys. Rev. D **41**, 2492 (1990).